Optical magnetic multimodality imaging of plectin-1-targeted imaging agent for the precise detection of orthotopic pancreatic ductal adenocarcinoma in mice

Wenjia Zhang,[a,c,1] Xiaolong Liang,[b,1] Liang Zhu,[a] Xinyu Zhang,[a] Zhengyu Jin,[a]* Yang Du,[c,d]** Jie Tian,[c,e]** and Huadan Xue[a]*

[a]Department of Radiology, State Key Laboratory of Complex Severe and Rare Diseases, Peking Union Medical College Hospital, Peking Union Medical College and Chinese Academy of Medical Sciences, No. 1 Shuaifuyuan, Dong Cheng District, Beijing 100730, China
[b]Department of Ultrasound, Peking University Third Hospital, Beijing 100191, China
[c]CAS Key Laboratory of Molecular Imaging, Beijing Key Laboratory of Molecular Imaging, the State Key Laboratory of Management and Control for Complex Systems, Institute of Automation, Chinese Academy of Sciences, No. 95 Zhongguancun East Road, Hai Dian District, Beijing 100190, China
[d]The University of Chinese Academy of Sciences, Beijing 100049, China
[e]Beijing Advanced Innovation Centre for Big Data-Based Precision Medicine, School of Medicine, Beihang University, Beijing 100191, China

eBioMedicine 2022;80: 104040
Published online xxx
https://doi.org/10.1016/j.ebiom.2022.104040

Summary

Background Pancreatic ductal adenocarcinoma (PDAC) is a lethal malignancy worldwide, and the precise detection is challenging currently. Magnetic particle imaging (MPI) is suitable for imaging deep and internal PDAC tumours because of its high sensitivity and unlimited imaging depth. The purpose of this study was to utilize the MPI, in combination with fluorescence molecular imaging (FMI) and magnetic resonance imaging (MRI), to advance the *in vivo* precise detection of PDAC xenografts.

Methods The PDAC targeted plectin-1 peptide and IRDye800CW were conjugated to the superparamagnetic iron oxide nanoparticles (PTP-Fe_3O_4-IRDye800CW) for the PDAC-targeting triple-modality imaging. Subcutaneous and orthotopic PDAC mouse models were established. FMI, MPI, and MRI were performed for dynamic and quantitative observation of PDAC tumours. Histological staining analyses were used for *ex vivo* validation.

Findings PTP-Fe_3O_4-IRDye800CW nanoparticles possessed great triple-modality imaging performance and specific targeting to plectin-1 expressed on PDAC cells. For *in vivo* multi-modality imaging of orthotopic PDAC models, the PTP-Fe_3O_4-IRDye800CW nanoparticles demonstrated higher specificity, even distribution, and longer retention effects in tumours for over 7 d compared with Con-Fe_3O_4-IRDye800CW nanoparticles. (MPI, 2d post-injection: PTP-Fe_3O_4-IRDye800CW: 85.72% ± 1.53% vs. Con-Fe_3O_4-IRDye800CW: 74.41% ± 1.91%, $^{**}P < 0.01$ (Student's *t* test)). *Ex vivo* histological and Prussian blue stainings were performed to validate the distribution of probes.

Interpretation These data demonstrate the feasibility of utilizing MPI for *in vivo* PDAC imaging and complement with FMI/MRI for a precise and comprehensive *in vivo* characterization of PDAC. This may benefit PDAC patients for precise diagnosis and guidance of therapy.

Funding This study was funded by the National Natural Science Foundation of China (Grant No. 62027901, 82071896, 81871422, 81871514, 81227901), Ministry of Science and Technology of China under Grant No. 2017YFA0205200, 2017YFA0700401, Beijing Natural Science Foundation (Grant No. 7212207), Elite Program of Dong Cheng District of Beijing (2020-dchrcpyzz-28), and Peking University Third Hospital (BYSYZD2019018, and jyzc2018-02).

*Corresponding author at: Department of Radiology, State Key Laboratory of Complex Severe and Rare Diseases, Peking Union Medical College Hospital, Peking Union Medical College and Chinese Academy of Medical Sciences, No. 1 Shuaifuyuan, Dong Cheng District, Beijing 100730, China
**Corresponding author at: CAS Key Laboratory of Molecular Imaging, Beijing Key Laboratory of Molecular Imaging, the State Key Laboratory of Management and Control for Complex Systems, Institute of Automation, Chinese Academy of Sciences, No. 95 Zhongguancun East Road, Hai Dian District, Beijing 100190, China.
E-mail addresses: jinzy@pumch.cn (Z. Jin), yang.du@ia.ac.cn (Y. Du), jie.tian@ia.ac.cn, tian@ieee.org (J. Tian), bjdanna95@hotmail.com (H. Xue).
[1] These authors contributed equally to this work.

Keywords: Pancreatic ductal adenocarcinoma (PDAC); Magnetic particle imaging (MPI); Superparamagnetic iron oxide nanoparticles (SPIONs); Fluorescence molecular imaging (FMI); Magnetic resonance imaging (MRI)

Research in context

Evidence before the study

Molecular imaging is an emerging and indispensable tool for diagnosis of pancreatic cancer at molecular and cellular level. Although optical imaging techniques and magnetic resonance imaging are widely used, magnetic particle imaging (MPI) is especially suitable for imaging tumours in deep organs due to its high sensitivity, unlimited imaging depth, and positive imaging signals. We searched PubMed and Web of Science for papers published from database inception to Nov, 2021, with the terms ("pancreatic cancer" OR "pancreatic tumor" OR "pancreatic tumour" OR "pancreatic ductal adenocarcinoma") AND ("magnetic particle imaging" OR "MPI"), with no language restrictions and source restrictions. To the best of our knowledge, there are no published studies so far that utilized MPI or multi-modality imaging including MPI to image pancreatic cancer.

Added value of the study

Our study utilized MPI for *in vivo* pancreatic cancer imaging and complemented with FMI/MRI for a more comprehensive *in vivo* characterization of PDAC mouse model, allowing for precise detection.

Implications of all the available evidence

Precise imaging of PDAC plays an important role in cancer diagnosis and therapy. Current available evidence implicates the combination of MPI with FMI/MRI triple-modality imaging can facilitate precision and high-resolution detection of orthotopic PDAC *in vivo*. Our triple-modality imaging approach for PDAC may have broad theranostic applications, such as sensitive tumour detection, delineation of tumour margin for intraoperative surgery, post-surgical follow-up imaging without repetitive administration of contrast agents, and guidance for targeted therapy such as magnetic hyperthermia therapy. Moreover, the main components of targeted nanoparticles are biocompatible materials, and hence, these nanoparticles possess potential for clinical translation for PDAC diagnosis and therapy in the future.

Introduction

Pancreatic cancer is one of the most fatal cancers globally and has the lowest 5-year survival rate of 9%.[1] Clinically, more than 80% of patients are diagnosed in the advanced stage and miss the opportunity for surgery.[2] In addition, some pancreatic ductal adenocarcinoma (PDAC) patients with a late diagnosis show a poor response to chemotherapy.[3] Therefore, early detection for aiding diagnosis is of great importance for improving therapeutic efficacy and patient survival rate.[4] However, it is difficult to detect PDAC using current clinical imaging methods such as computed tomography (CT) and magnetic resonance imaging (MRI), especially when it is located in the deep retroperitoneal space. Consequently, there is an urgent need to identify new and promising imaging methods.

Molecular imaging is an emerging and indispensable tool for diagnosis and treatment of PDAC and it can detect diseases at the molecular and cellular levels.[5–7] However, each imaging modality has strengths and limitations. Optical imaging techniques, for example, fluorescence molecular imaging (FMI), show the advantages of high sensitivity and spatial resolution, and they can monitor the real-time pharmacokinetics and biodistribution of nanoparticles in the whole body. But FMI is limited by the low imaging depth due to the light absorption and scattering.[8] MRI can provide morphological and anatomical details of deep tissues with excellent resolution and is widely used in clinics. Despite the application of contrast agent in MRI, the sensitivity of MRI is still limited.[9,10] Therefore, it is of great importance to develop multimodal imaging, which can integrate complementary advantages of different imaging modalities.

Magnetic particle imaging (MPI) is a promising imaging technique that was utilized by Elaine et al. for cancer detection in 2017.[11,12] MPI is a tomographic imaging technique that detects the change in iron electronic magnetization, while MRI measures the change in water proton nuclear magnetization. Hence, MPI offers much higher sensitivity than MRI, with nearly no background signal and negligible tissue attenuation.[11,13] MPI is superior in its ability to directly detect the amount of SPIONs and provide positive signals.[14,15] MPI can also non-invasively and quantitatively monitor the biodistribution of tracers with no ionising radiation.[12] However, MPI shows low spatial resolution and no anatomical information; Hence, the combination of MPI with FMI and MRI can complement the respective imaging strengths and provide more accurate and deeper anatomical details for the precise imaging and

detection of PDAC.[16] To realize the above purpose, the development of a corresponding triple FMI/MPI/MRI imaging agent is needed.

SPIONs are common imaging agents for MPI/MRI and provide an excellent nanoplatform for imaging various tumours, and some of them have entered clinical trials.[17–19] Targeted SPIONs conjugated with specific ligands, including antibodies, peptides, and nucleotides, are considered ideal imaging probes with high biocompatibility and low toxicity.[20–24] Recent studies have shown that some biomarkers were successfully applied and improved the targeted and specific detection of PDAC in preclinical research. Among them, plectin-1 is a promising biomarker for pancreatic cancer. Kelly et al. found that this targeted molecule was over-expressed in invasive pancreatic cancer.[25] Bausch et al. demonstrated that 93% of PDAC cases were plectin-1 positive.[26] Furthermore, plectin-1 could distinguish malignant from benign cancer lesions with 84% sensitivity and 83% specificity. Plectin-1 is recognized as a biomarker of invasive and metastatic PDAC, and also a biomarker of pre-invasive pancreatic intraepithelial neoplasia (PanIN)-III lesions.[26] Therefore, plectin-1 may be a promising biomarker for specific and targeted PDAC imaging.

In this study, we designed and synthesized plectin-1 peptide (PTP)-targeted and near-infrared dye IRDye800CW-conjugated SPIONs, abbreviated as PTP-Fe_3O_4-IRDye800CW, using Con-Fe_3O_4-IRDye800CW nanoparticles as a control. PTP-Fe_3O_4-IRDye800CW was applied to both the subcutaneous and orthotopic PDAC mouse models for FMI/MPI/MRI multimodality imaging (Figure 1). We found that PTP-Fe_3O_4-IRDye800CW showed even distribution and longer retention in PDAC compared with the Con-Fe_3O_4-IRDye800CW, which was restricted only to the injection site. In general, our PTP-Fe_3O_4-IRDye800CW multimodality imaging probe showed more sensitive

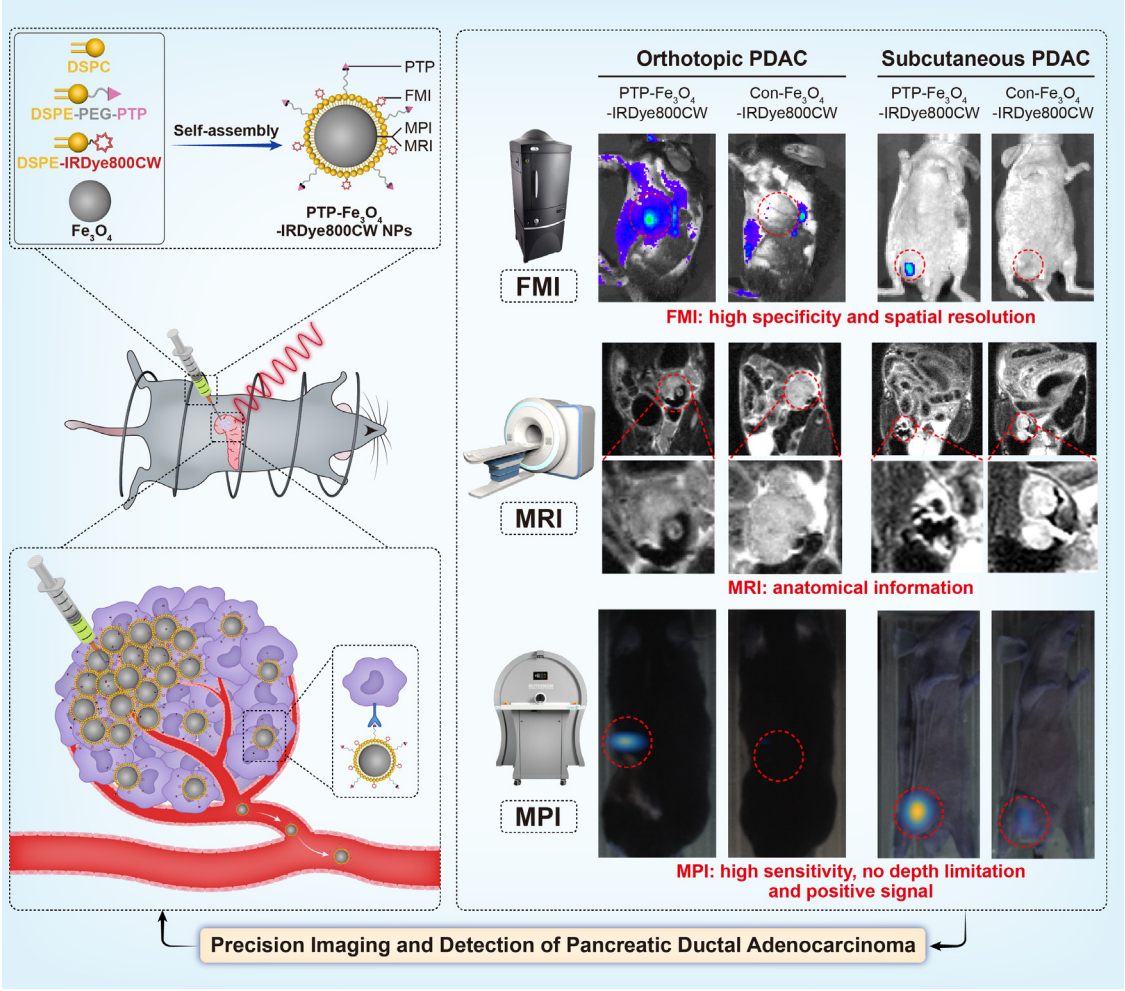

Figure 1. Schematic illustration of the multimodality imaging of orthotopic and subcutaneous PDAC using a targeted PTP-Fe_3O_4-IRDye800CW imaging agent. Multimodality imaging includes FMI, MPI and MRI.

detection of PDAC with outstanding targeting ability and exhibited good safety. In conclusion, this study uses MPI for *in vivo* pancreatic cancer imaging and complements with FMI/MRI for a more comprehensive *in vivo* characterization of PDAC, allowing for precise detection.

Methods

Ethics

All experiments were performed under the approval of the Ethics Committee at the Chinese Academy of Medical Sciences and Peking Union Medical College (Permit number: JS2591).

Synthesis of DSPE-IRDye800CW

DSPE-IRDye800CW was synthesized according to a previously reported method.[27] Briefly, DSPE and IRDye800CW NHS ester with a molar ratio of 1.15:1 were dissolved in a mixture of dimethyl sulfoxide (DMSO), $CHCl_3$, and TEA at a volume ratio of 1:2:0.06, followed by overnight incubation at 35°C in the dark. After incubation, the organic solvent was evaporated to dryness, and the resulting product was purified using an FPLC HiTrap column with water as the eluent.

Synthesis of DSPE-PEG-PTP

DSPE-PEG-PTP was synthesised by conjugating the amino group of PTP with DSPE-PEG-NHS ester via amide bonds.[28] Briefly, DSPE-PEG-NHS and PTP were mixed in a 1:2 molar ratio in an aqueous buffer solution (pH 8.5–9.0), followed by incubation at 37 °C for 4 h. The resulting mixture was purified using a dialysis bag with a molecular weight cut-off of 8,000–14,000 to remove unconjugated PTP, lyophilised, and stored at −20 °C until further use. DSPE-PEG-Con was synthesised in a similar manner.

Preparation of PTP-Fe_3O_4-IRDye800CW nanoparticles

The sequence of PTP polypeptides was KTLLPTP (Nanjing TGpeptide Biotechnology Co., Ltd, China). Control polypeptides were synthesized randomly with almost the same relative molecular mass as the PTP peptides containing the GTDYEW sequence (Nanjing TGpeptide Biotechnology Co., Ltd, China). The self-assembly method was used to fabricate PTP- and IRDye800CW-modified Fe_3O_4 through hydrophobic forces. Briefly, oleic acid-modified Fe_3O_4 and phospholipids (containing DSPE-PEG-PTP, DSPE-IRDye800CW, and DSPC at a molar ratio of 30:10:60) were mixed in chloroform at a mass ratio of 1:2 and ultrasonically agitated to ensure that Fe_3O_4 was well dissolved. The sample was then slowly evaporated with nitrogen at 25 °C to form a thin film on the vial, followed by the addition of 2 mL water and vigorous sonication for 1 h. The sample was then filtered through a nylon filter (0.45 μm) to remove large aggregates. The filtrate was centrifuged (25,000 rpm. for 0.5 h × 3 times) to collect aqueous PTP-Fe_3O_4-IRDye800CW. IRDye800CW and Fe_3O_4 concentrations were determined by measuring the filtrates, supernatants, and resuspended pellets via fluorescence spectra and ICP-OES. Con-Fe_3O_4-IRDye800CW nanoparticles were prepared using the same procedure. The zeta potential value of PTP-Fe_3O_4-IRDye800CW and Con-Fe_3O_4-IRDye800CW were characterized using a Zetasizer Nano ZS90 at room temperature.

Cell culture

The murine pancreatic cancer cell line Pan02 (NCI-DTP Cat# PAN 02, RRID: CVCL_D627) and human pancreatic cancer cell line BxPC3 (DSMZ Cat# ACC-760, RRID: CVCL_0186) were gifted by the Radiology Department of Peking Union Medical College Hospital, China. Human pancreatic ductal epithelial cells HPDE6-C7 (BFN60807571) was purchased from Bluefbio (Shanghai) Biology Technology Development Co., Ltd. The PDAC cells were transfected with luciferase gene and used for all subsequent experiments as BxPC3-Luc and Pan02-Luc. RPMI 1640 medium, high-glucose DMEM and fetal bovine serum (FBS) were bought from HyClone (Thermo Scientific, Waltham, MA, USA). The cells were cultured in RPMI 1640 medium and high-glucose DMEM containing 10% FBS and 1% penicillin/streptomycin at 37 °C in 5% CO_2.

Plectin-1 expression validation

Tumour examples of Pan02 and BxPC tumour-bearing mice and normal mice were obtained to process plectin-1 immumohistochemical staining. Paraffin-embedded sections were deparaffinized and hydrated, and then antigen retrieval by boiling tissue. Endogenous peroxidase activity was blocked and serum were sealed by 3% BSA (G5001, Servicebio, Wuhan, China). Primary anti-plectin-1 antibody (Bosterbio, #PB9430, Pleasanton, CA, USA) and goat polyclonal secondary antibody to rabbit IgG-HRP (GB23303; Servicebio, Wuhan, China) were successively incubated. DAB color developing solution were added and treated with hematoxylin returning blue solution. Slides were observed using a DS-U3 microscope (Nikon).

Pan02 and BxPC3 cells were resuspended in 0.5 mL phosphate-buffered saline (PBS) to do flow cytometry analysis. The cells were cultured with anti-plectin antibody Picoband™ (Bosterbio, #PB9430, Pleasanton, CA, USA) and goat polyclonal secondary antibody to rabbit IgG-H&L (Alexa Fluor® 488) (Abcam, Cambridge, UK; Abcam Cat# ab150077, RRID: AB_2630356) or an isotype-matched negative control antibody (Abcam Cat#

ab37415, RRID: AB_2631996) for 30 min at 4 °C. Analysis was performed using the BD LSRII flowcytomter (BD Biosciences, San Jose, CA, USA).

As for western blot, 20 μg of protein from BxPC-3 and HPDE6-C7 cell lines and pancreas tissues of health mice and PDAC tissues of Pan02 orthotopic tumour-bearing mice were loaded on a 5% and 10% sodium dodecyl sulfate–polyacrylamide gel for plectin-1 and β-Actin, respectively for both about 2 h at 120 v. Then the samples were transferred to polyvinylidene difluoride membranes, which was then blocked with 5% (w/v) skim milk at room temperature for about an hour and incubated with an anti-plectin-1 primary monoclonal antibody (Cell Signaling Technology Cat# 12254, RRID: AB_2797858) at 4 °C overnight. The samples were washed in TBST for three times, and incubated with a secondary antibody conjugated with goat polyclonal secondary antibody to rabbit IgG-HRP (GB23303; Servicebio, Wuhan, China) for about 1 h at room temperature. The bands were analysed by enhanced chemiluminescence (ImageQuant LAS 500, GE, USA).

The cytotoxicity of nanoparticles

Pan02, BxPC3 and HPDE6-C7 cells were seeded (approximately 2,000 cells/well) in 96-well plates and incubated with various concentrations of PTP-Fe_3O_4-IRDye800CW nanoparticles and controlled medium for 24 h. Then the cells were washed with PBS for three times and treated with 100 μL 1640 containing 10 μL CCK-8 solution for 2 h. Optical density values were analyzed at 450 nm then the quantitative values were measured by a microplate reader (Synergy HT Multi-Mode Microplate Reader, Biotek, Winooski, VT, USA).

Evaluation of *in vitro* targeting specificity

For confocal microscopy imaging, Pan02 and BxPC3 cells were seeded (approximately 1×10^5 cells/well) in 20 mm glass-bottom dishes for 24 h. Afterwards, the medium was replaced by 1 mL fresh medium containing 10 μL 1 mg/mL PTP-Fe_3O_4-IRDye800CW or Con-Fe_3O_4-IRDye800CW nanoparticles. After 2 h incubation, the cells were washed with cold PBS, fixed using 4% paraformaldehyde, and stained with DAPI (Solarbio, Beijing, China). Light was avoided during the entire process. Images were obtained using confocal laser scanning microscope (LSM780, Carl Zeiss, Jena, Germany). For flow cytometry analysis, the cells were resuspended in cell staining buffer, and the cell concentration was adjusted to 1×10^7 cells/mL. 100 μL of cell suspension (10^6 cells) was added to 500 μL of fixation buffer, mixed and incubated at room temperature for 20 min. 2 mL of membrane permeation washing solution was added to the tube, and then resuspend the cells in 100 μL of membrane permeation washing solution. 1 μg of PTP-Fe_3O_4-FITC and Con-Fe_3O_4-FITC were incubated for 0.5 h, respectively. Membrane permeation wash solution and flow cytometry staining solution were added. Analysis was performed using the BD LSRII flowcytomter (BD Biosciences, San Jose, CA, USA).

Animal experiments

Six-week-old BALB/c nude mice and C57BL/6N mice were purchased from the Charles River Laboratory Animal Technology Corporation, Beijing, China. For the subcutaneous mouse model, the mice were anaesthetised with 1.5% isoflurane. Then, BxPC3-Luc tumour cells (1.5×10^6) were subcutaneously injected with 100 μL cell suspension in Matrigel directly into the right groin region of each mouse. For the orthotopic mouse model, Pan02-Luc tumour cells (2×10^6) were injected with 25 μL cell suspension in Matrigel into the tail of the pancreas of C57BL/6N mice via abdominal surgery. The tumour-bearing mice were divided into two groups randomly when their tumour volume reached approximately 100 mm^3, as follows: Con-Fe_3O_4-IRDye800CW group; PTP- Fe_3O_4-IRDye800CW group. Twenty-five microliters of 1 mg/mL nanoparticles were intratumourally injected into each group before multi-modality imaging. For the subcutaneous mouse model, intratumoural injection was administrated percutaneously after skin-sterilizing. For the orthotopic mouse model, intratumoural injection was administrated through surgical operation after anesthesia. Multi-modality imaging was performed throughout 7 d, including *ex vivo* imaging at 2 d for FMI and MPI.

Bioluminescence imaging

The establishment of an orthotopic PDAC mouse model was verified using bioluminescence imaging (BLI). C57BL/6N mice were anaesthetised with 1.5% isoflurane and oxygen and then intraperitoneally administered D-luciferin (Perkin Elmer, Waltham, MA, USA) (150 μg/g body weight) 8 min prior to imaging. BLI images were captured using an IVIS spectrum (PerkinElmer, Waltham, MA, USA) to examine the location of the tumour compared to the FMI signals. Comparison of the location of FMI signals was conducted to further identify the establishment of an orthotopic mouse model. At 2 d after injection, the mice were euthanised followed by excision of tumours and major organs for *ex vivo* BLI.

Fluorescence molecular imaging (FMI)

As for fluorescence stability of PTP-Fe_3O_4-IRDye800CW nanoparticles, 100 μL of 3.75 μg/ml, 7.5 μg/ml, 15 μg/ml probes were placed into 96-well plates, respectively. Images were captured by IVIS spectrum at excitation and emission wavelengths of 745 and 840 nm for every two or three days over 16 days. For *in vitro* FMI, probes at different concentrations from

0.3125 to 25.00 mg/mL were placed into 96-well plates, respectively for capturing by IVIS.

Isoflurane-anaesthetized mice underwent FMI after intratumoural injection of Con-Fe_3O_4-IRDye800CW or PTP-Fe_3O_4-IRDye800CW (IVIS spectrum). Images were captured pre-injection and after 4 h, 8 h, 12 h, 24 h, 2 d, 3 d, 5 d, and 7 d at excitation and emission wavelengths of 745 and 800 nm. At 2 d post-injection, the tumour-bearing mice of each group were euthanised to obtain the major organs (heart, liver, spleen, lung, kidney, and tumour), for *ex vivo* imaging. The Living Image 4.4 Software (PerkinElmer, Waltham, MA, USA) was used to analyze the results quantitatively. All mice were analysed by calculating the normalised fluorescence intensity (NFI) as follows: NFI (%) = (TFIx / BFIx)/ (TFI_o / BFI_o) × 100%, where TFIx is the average fluorescence intensity of the region of interest (ROI) of the tumour at each time point after injection, and BFIx is the background fluorescence intensity, which is represented by the ROI of the muscle area at different time points; BFI_o and TFI_o represent the average fluorescence intensity of the background and tumour areas of the ROI at 4 h after nanoparticles injection, respectively.

Magnetic particle imaging (MPI)

MPI was carried out on a MOMENTUM MPI scanner (Magnetic Insight, Inc., Alameda, CA, USA). For *in vitro* MPI, probes at different concentrations from 1.0 to 2.0 mg/mL were placed in eppendorf tubes for scanning (parameters: *Z* field of view (FOV), 4 cm; mode, isotropic; and time estimate, 2 min). For *in vivo* imaging, all mice were anaesthetised with 1.5% isoflurane and underwent two-dimensional (2D) MPI at 4 h, 8 h, 12 h, 24 h, 2 d, 3 d, 5 d, and 7 d after injection (parameters: Z FOV, 12 cm; mode, isotropic; and time estimate, 2.8 min). Three-dimensional (3D) MPI was carried out at 48 h post-injection (parameters: Z FOV, 12 cm; mode, isotropic; projection number, 35; and time estimate, 45 min). CT was performed on a homemade micro-CT scanner in normal scan mode (parameters: voltage, 50 kV; current, 800 μA; FOV, 120 × 120 × 120 mm; and scan time, 7 min). 3D reconstruction, co-registration, and quantification analysis of the MPI/CT images were performed using the Vivo-Quant 4.0 software (Invicro, Boston, MA, USA). All mice were analysed by calculating the normalised MPI signals (NMS) as follows: NMS (%) = (TMSx / BMSx) / (TMS_o / BMS_o) × 100%, where TMSx is the average MPI signal within the ROI of the tumour at each time point after injection, and BMSx is the background MPI signal, which is represented by the ROI of the muscle area at different time points; BMS_o and TMS_o are the average MPI signals within the ROI of the background and tumour areas at 4 h post-injection, respectively.

Magnetic resonance imaging (MRI)

The transverse (T2) relaxation times of nanoparticles (Con-Fe_3O_4-IRDye800CW or PTP-Fe_3O_4-IRDye800CW) were evaluated at incremental concentrations (0.01625–0.25 mg/mL) at 20 °C using a 7.0 T small animal MRI scanner (BioSpec 70/20 USR; Bruker, Billerica, MA, USA). The parameters were as follows: FOV, 40 × 40 mm; slice thickness, 1 mm; TR, 3,000 ms; and TE, 40 ms.

All mice were scanned using a 1.5 T M3TM MRI imager (Aspect Imaging, Shoham, Israel) with a 38 mm body coil. The mice were anaesthetised using a 1.5% isoflurane and oxygen mixture. MRI images were captured using a T2-Turbo RARE sequence (parameters: TR, 5557 ms; TE, 66.61 ms; FOV, 30 × 60 mm; slice orientation, coronal; and thickness, 0.8 mm). To observe the changes at the tumour site, MRI images were acquired before injection and at 4 h, 12 h, 24 h, 2 d, 3 d, 5 d, and 7 d post-injection.

***Ex vivo* histology, Prussian blue staining, and evaluation of liver/kidney function.** After *ex vivo* FMI and MPI, the major organs and tumours were immersed in 10% formalin then embedded in paraffin. Haematoxylin and eosin (H&E) and Prussian blue stainings were conducted to analyse the biotoxicity and distributions of nanoparticles. CD31 staining using anti-CD31 antibody (GB13428; Servicebio, Wuhan, China) and goat polyclonal secondary antibody to rabbit IgG-HRP (GB23303; Servicebio, Wuhan, China) was conducted to analyse the location of vascular endothelial cells. Images were processed and digitalised using a digital slide scanner (Pannoramic 250 Flash III, 3D Histech, Hungary).

At 7 d post-injection, the blood samples were collected and stored for 2 h at 20 °C and then centrifuged at 3,500 rpm for approximately 15 min to separate serum samples. Alanine transaminase (ALT), aspartate transaminase (AST), alkaline phosphatase (ALP), blood urea nitrogen (BUN), and creatinine (Cr) levels were evaluated on a chemistry analyzer (Chemray-240, Rayto, Shenzhen, China).

***In vitro* magnetic hyperthermia.** Magnetic hyperthermia of PTP-Fe_3O_4-IRDye800CW at a concentration of 1 mg/ml (Fe) in 500 µL aqueous solution was performed by applying an alternating magnetic field at 495 kHz and 20 A. The heating curve over time was monitored by an optical fiber probe thermometer.

Statistical analysis

GraphPad Prism software (GraphPad Prism 6.0, Inc., La Jolla, CA, USA) was used to run statistical analysis. Data are presented as the mean ± SD. For comparisons between two groups, statistical significance was assessed by Student's *t* test (*$P < 0.05$ considered

significant). *, **, ***, and **** represent $P < 0.05$, $P < 0.01$, $P < 0.001$, and $P < 0.0001$, respectively. For comparisons between three groups, statistical significance was assessed by one-way ANOVA (*$P < 0.05$ considered significant).

Reagent validation

All cells in this study were routinely inspected for their recognizable morphology in a light microscope, short tandem repeat (STR) profiling and recent mycoplasma testing have been performed by well-established commercial vendors as shown in Supplementary Materials (Reagent Validation file). All antibodies in this study were commonly commercial used. They were purchased from commercial vendors and matched for the molecular weight of the antibody to the corresponding data sheet provided by the supplier. The detailed information of cell lines and antibodies is available in the Supplementary Materials.

Role of the funding source

The funders of the manuscript had no role in the study design, data collection, data analyses, data interpretation, or writing of the manuscript.

Results

Characterization of PTP-Fe_3O_4-IRDye800CW nanoparticles

To ensure active targeting, DSPE-PEG-PTP and DSPE-PEG-CON were first synthesised by conjugating PTP to DSPE-PEG-NHS with an active carbonyl ester group via stable amide bonds, which was demonstrated using Fourier-transform infrared spectroscopy (FTIR) spectra (Supplementary Figure 1a, b). Transmission electron microscopy (TEM) observation demonstrated that the uniform size of PTP-Fe_3O_4-IRDye800CW nanoparticles was ~20 nm with square morphology (Figure 2a), and dynamic light scattering revealed an average particle size of 27.2 nm (Supplementary Figure 1c). The slightly larger size is likely due to the surface coating layer, which disrupts nanoparticle aggregation. The Con-Fe_3O_4-IRDye800CW was similar in size (~25.6 nm) and morphology (Figure 2b, Supplementary Figure 1d). The FTIR spectra displayed characteristic peaks of DSPE-PEG-PTP or DSPE-PEG-CON and DSPE-IRDye800CW, which indicated successful modifications of the targeting group and fluorescent dye onto the nanoparticles (Figure 2c, d). In addition, the zeta potentials of PTP-Fe_3O_4-IRDye800CW and Con-Fe_3O_4-IRDye800CW were measured, showing similar zeta potentials of about -12.25 mV and -13.82 mV, respectively.

The absorbance spectra of aqueous PTP-Fe_3O_4-IRDye800CW and Con-Fe_3O_4-IRDye800CW nanoparticles exhibited a wide and elevated absorption between 550and 850 nm and a maximum absorption at ~780 nm, which was slightly red-shifted compared to that of the free IRDye800CW. The highest peak was at 774 nm (Figure 2e). This shift might be due to the interaction between IRDye800CW and the cored Fe_3O_4. The IRDye800CW fluorescence emission spectra further indicated that both PTP-Fe_3O_4-IRDye800CW and Con-Fe_3O_4-IRDye800CW nanoparticles showed similar fluorescence as free IRDye800CW upon light irradiation (the excitation and emission wavelengths were 740 nm and 795 nm, respectively) (Figure 2f). PTP-Fe_3O_4-IRDye800CW nanoparticles were well dispersed in various biological media with no precipitation (Supplementary Figure 1e). In addition, we monitored the fluorescence intensities of PTP-Fe_3O_4-IRDye800CW in 3.75 μg/ml, 7.5 μg/ml, 15 μg/ml concentrations over 16 d. The observations demonstrated the probe has great stability in our study (Supplementary Figure 1f). These findings revealed that it can be further utilized for the following imaging studies.

***In vitro* FMI/MPI/MRI properties of PTP-Fe_3O_4-IRDye800CW.** To assess the FMI, MPI, and MRI T2 relaxivity properties of PTP-Fe_3O_4-IRDye800CW nanoparticles, we initially conducted measurements in phantom. PTP-Fe_3O_4-IRDye800CW nanoparticles were prepared at different Fe concentrations to analyse the relevance of FMI, MPI, and MRI. As shown in Figure 2g, the fluorescence intensity was linearly correlated with the increased concentration of PTP-Fe_3O_4-IRDye800CW samples at Fe concentrations ranging from 0.3125 to 2.5000 μg/mL. However, with the increase of sample concentration, the fluorescence intensity tended to reach a plateau at 20.00 μg/mL due to the quenching effect. The MPI linear regression results and corresponding images are demonstrated in Figure 2h, which shows that MPI signals increased with an increase of sample concentration. Moreover, Figure 2i shows the T2-weighted MRI of nanoparticles with reference to the sample concentration. The T2-weighted MR images of all the samples became dimming with incremental concentrations of contrast agents. The r_1 of PTP-Fe_3O_4-IRDye800CW nanoparticles was calculated to be 44.4192 $mM^{-1}s^{-1}$ at 7.0 T.

Characterization of plectin-1 expression

To validate plectin-1 as a specific imaging target for PDAC, its expression was analysed on human and murine PDAC cell lines and tumour tissues. In BxPC3 human PDAC xenografts obtained from nude mice, high plectin-1 expression levels were detected (Figure 3a). Similarly, plectin-1 was observed highly expressed in pano2 murine PDAC xenografts (Figure 3a). We found that plectin-1 was expressed at a

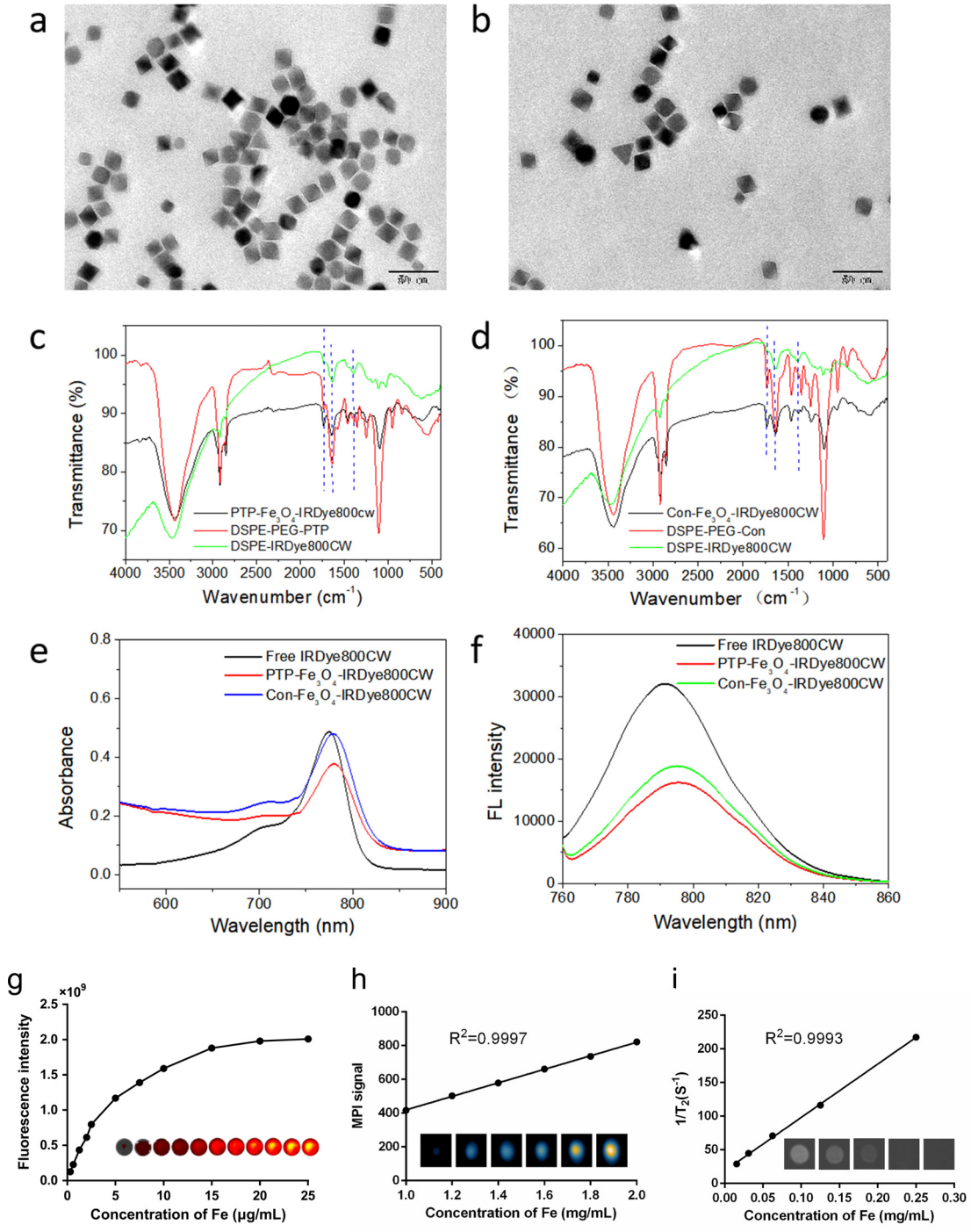

Figure 2. Characterization of PTP-Fe_3O_4-IRDye800CW imaging nanoparticles. Transmission electron microscopy images of (a) PTP-Fe_3O_4-IRDye800CW and (b) Con-Fe_3O_4-IRDye800CW nanoparticles (scale bar: 50 nm). (c) Fourier-transform infrared spectrometry (FTIR) spectra of PTP-Fe_3O_4-IRDye800CW and (d) Con-Fe_3O_4-IRDye800CW nanoparticles. (e) Absorbance spectra and (f) fluorescence of PTP-Fe_3O_4-IRDye800CW nanoparticles. Con-Fe_3O_4-IRDye800CW and free IRDye800CW nanoparticles were used as controls. (g) Fluorescence intensity of PTP-Fe_3O_4-IRDye800CW nanoparticles increased with rising fluorophore concentrations using the IVIS spectrum. (h) Magnetic particle imaging (MPI) signals of PTP-Fe_3O_4-IRDye800CW nanoparticles increased with rising Fe concentrations. (i) Transverse (T2)-weighted MR images of PTP-Fe_3O_4-IRDye800CW nanoparticles at varying Fe concentrations.

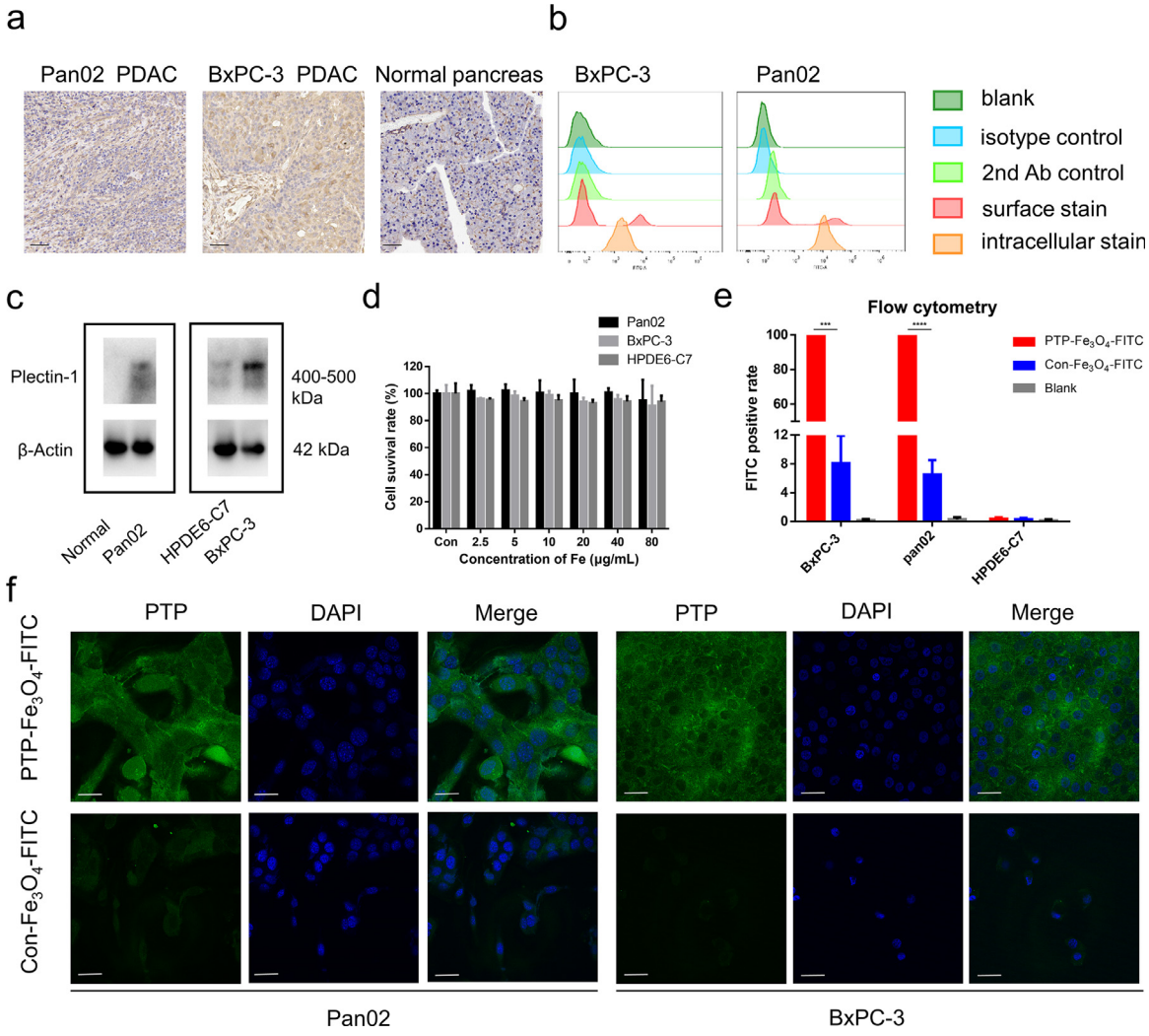

Figure 3. Examination of plectin-1 expression on PDAC and the targeting specificity, and cytotoxicity of PTP-Fe_3O_4-IRDye800CW nanoparticles. (a) High levels of plectin-1 expression were detected by immunohistochemical staining in pancreatic tumour tissues from Pan02 and BxPC3 tumour xenografts but not on normal pancreatic tissues from healthy mice (scale bar: 50 μm). (b) Plectin-1 expression in BxPC3 and Pan02 PDAC cell lines was determined by flow cytometry. (c) Western blot analysis of plectin-1. (d) *In vitro* cytotoxicity of Pan02 and BxPC3 cells incubated with increasing concentrations of PTP-Fe_3O_4-IRDye800CW nanoparticles. (e) Flow cytometry of targeting ability of PTP-Fe_3O_4-FITC in BxPC-3, Pan02 and HPDE6-C7 cells. (n = 3, respectively; one-way ANOVA; *, $P < 0.05$; **, $P < 0.01$; ***, $P < 0.001$, ****, $P < 0.0001$). (f) Panc02 and BxPC3 cells were incubated with PTP-Fe_3O_4-FITC and Con-Fe_3O_4-FITC nanoparticles for 4 h for laser scanning confocal microscopy (scale bar: 25 μm).

high level in PDAC but not in other major organs, such as heart, liver, spleen, lung, and kidney (Supplementary Figure 2a). The cell surface and intracellular expression of plectin-1 in the PDAC cell lines was quantified using flow cytometry. In Pan02 cells, 21.11% of plectin-1 expression was observed on the cell surface, and 90.05% was observed intracellularly. Similarly, 29.27% of the plectin-1 expression was observed on the BxPC3 cell surface, and 99.80% of the plectin-1 expression was observed intracellularly (Figure 3b). Moreover, we further analyzed the expression of plectin-1 using western blot in human pancreatic ductal epithelial cell lines (HPDE6-C7) and BxPC-3 PDAC cell lines, and in pancreas tissues of healthy mice and PDAC tissues of Pan02 orthotopic tumour-bearing mice. The observation of western blot clearly demonstrated that plectin-1 is overexpressed in human PDAC cell lines and murine PDAC tissues (Figure 3c).

***In vitro* targeting specificity and cytotoxicity of PTP-Fe_3O_4-IRDye800CW nanoparticles.** Cells were incubated with different concentrations of nanoparticles (2.5–80 μg/mL) for 24 h and their viability was

examined. The data showed that no significant cytotoxicity was observed (Figure 3d). As for *in vitro* targeting specificity, Pan02, BxPC-3 and HPDE6-C7 cells were incubated with PTP-Fe_3O_4-FITC and Con-Fe_3O_4-FITC for flow cytometry. As shown in Figure 3e, more than 99% of two PDAC cell lines were FITC-positive, while merely less than 1% of HPDE6-C7 cells were FITC-positive. Moreover, there was a significantly statistical difference between Con-Fe_3O_4-FITC and blank group (only cells without probes) as control respectively. The outcome demonstrated the outstanding targeting ability of PTP (Supplementary Figure 2b). Further, the binding specificity of PTP for both murine (Pan02-Luc) and human (BxPC3-Luc) PDAC cells was assessed. The PDAC cell uptake was obviously higher for PTP-Fe_3O_4-FITC nanoparticles than for Con-Fe_3O_4-FITC, which confirmed the specific PDAC cell targeting ability of the PTP peptide (Figure 3f). The cytotoxicity assay was analyzed using the CCK-8 assay in normal and cancer cells. The data showed that PTP-Fe_3O_4-IRDye800CW nanoparticles possessed good biocompatibility and biosafety.

***In vivo* MPI, FMI and MRI multimodality imaging for subcutaneous PDAC mouse model.** MPI-FMI-MRI triple-modality imaging was initially performed on an *in vivo* subcutaneous PDAC model. After intratumoural injection of PTP-Fe_3O_4-IRDye800CW or Con-Fe_3O_4-IRDye800CW nanoparticles (n = 3, respectively), the FMI data demonstrated that PTP-Fe_3O_4-IRDye800CW showed the highest fluorescence intensity at 4 h post-injection and almost equal fluorescence intensity with Con-Fe_3O_4-IRDye800CW nanoparticles, but the fluorescence intensity decreased at 8 h post-injection. The FMI data demonstrated that PTP-Fe_3O_4-IRDye800CW also had a longer retention effect compared to the Con-Fe_3O_4-IRDye800CW nanoparticles (Figure 4a). Quantitative analysis of the fluorescence intensity data was identical with the *in vivo* observation (Figure 4b). The difference between the two groups of NFI (%) appeared at 2 d (PTP-Fe_3O_4-IRDye800CW group: 43.68% ± 5.72% vs. Con-Fe_3O_4-IRDye800CW group: 31.79% ± 4.65%, $^*P < 0.05$ (Student's t test)), and we detected the NFI (%) until 7 d in the PTP-Fe_3O_4-IRDye800CW group (PTP-Fe_3O_4-IRDye800CW group: 30.41% ± 7.77% vs. Con-Fe_3O_4-IRDye800CW group: 13.13% ± 0.44%, $^*P < 0.05$ (Student's t test)). These results demonstrated that PTP-Fe_3O_4-IRDye800CW imaging nanoparticles showed targeted imaging and longer retention effects than Con-Fe_3O_4-IRDye800CW in the tumours.

Moreover, subcutaneous models were simultaneously monitored using MPI. MPI signal changes were observed for both PTP-Fe_3O_4-IRDye800CW and Con-Fe_3O_4-IRDye800CW nanoparticles 4 h post-injection (Figure 4c) (n = 3, respectively). Similarly, the MPI signals of the PTP-Fe_3O_4-IRDye800CW group was metabolised relatively slower compared with Con-Fe_3O_4-IRDye800CW nanoparticles as 2 d (PTP-Fe_3O_4-IRDye800CW group: 87.90 ± 5.55% vs. Con-Fe_3O_4-IRDye800CW group: 64.91 ± 6.97%, $^{**}P < 0.01$ (Student's t test)). The PTP-Fe_3O_4-IRDye800CW group demonstrated longer retention until 7 d, which possessed 1.45-fold of MPI signals higher of Con-Fe_3O_4-IRDye800CW group (PTP-Fe_3O_4-IRDye800CW group: 72.66 ± 3.27% vs. Con-Fe_3O_4-IRDye800CW group: 49.95 ± 7.98%, $^*P < 0.05$ (Student's t test)) (Figure 4d).

As the representative clinical imaging modality, MRI was also performed. The results in Figure 4e distinctly show that T2-weighted signals for the PTP-Fe_3O_4-IRDye800CW targeting probe in the coronal position gradually diffused through the whole PDAC xenografts, but the MRI signal was restricted to the injection site for the Con-Fe_3O_4-IRDye800CW group (n = 3, respectively). Notably, the increased darker T2-weighted signals and prolonged retention caused by the PTP-Fe_3O_4-IRDye800CW targeting probe were retained for 7 d post-injection (red dotted circle showed the tumour, blue dotted line drew the outline of nanoparticles area). By contrast, Con-Fe_3O_4-IRDye800CW probe stayed at the injection site for a short period of time and then showed rapid washout. MRI offers anatomical details, and can locate the probe position within the tumour site.

To verify the *in vivo* triple-modality imaging observations, the tumours and major organs were obtained for further *ex vivo* multimodality imaging. As shown in Figure 5a, *ex vivo* FMI images of the tumours and major organs were obtained at 2 d. Stronger fluorescence intensity of tumour was observed in the PTP-Fe_3O_4-IRDye800CW group than Con-Fe_3O_4-IRDye800CW group. We further performed *ex vivo* MPI scanning at 2 d. Tumours in the PTP-Fe_3O_4-IRDye800CW group had stronger MPI signal than the Con-Fe_3O_4-IRDye800CW group (Figure 5b) (PTP-Fe_3O_4-IRDye800CW: 111.84 ± 1.31 vs. Con-Fe_3O_4-IRDye800CW: 100.08 ± 0.04, $^{***}P < 0.001$ (Student's t test)) (Supplementary Figure 3a). Finally, histological and Prussian blue stainings were performed, and the data showed that more Fe-positive staining was evenly distributed inside the tumour in the PTP-Fe_3O_4-IRDye800CW group than the Con-Fe_3O_4-IRDye800CW group (Figure 5c). Furthermore, the liver and spleen tissues of the Con-Fe_3O_4-IRDye800CW group showed a small amount of Fe-positive staining in sporadic areas, but Fe-positive staining was barely detected in the PTP-Fe_3O_4-IRDye800CW group. For the biosafety evaluation, we performed H&E staining of the major organs as well as liver and renal function in PTP-Fe_3O_4-IRDye800CW and normal saline group. No abnormalities were found in major organs, as heart, liver, spleen, lung, and kidney (Supplementary Figure 4a). In addition, ALT, AST, and ALP were tested for

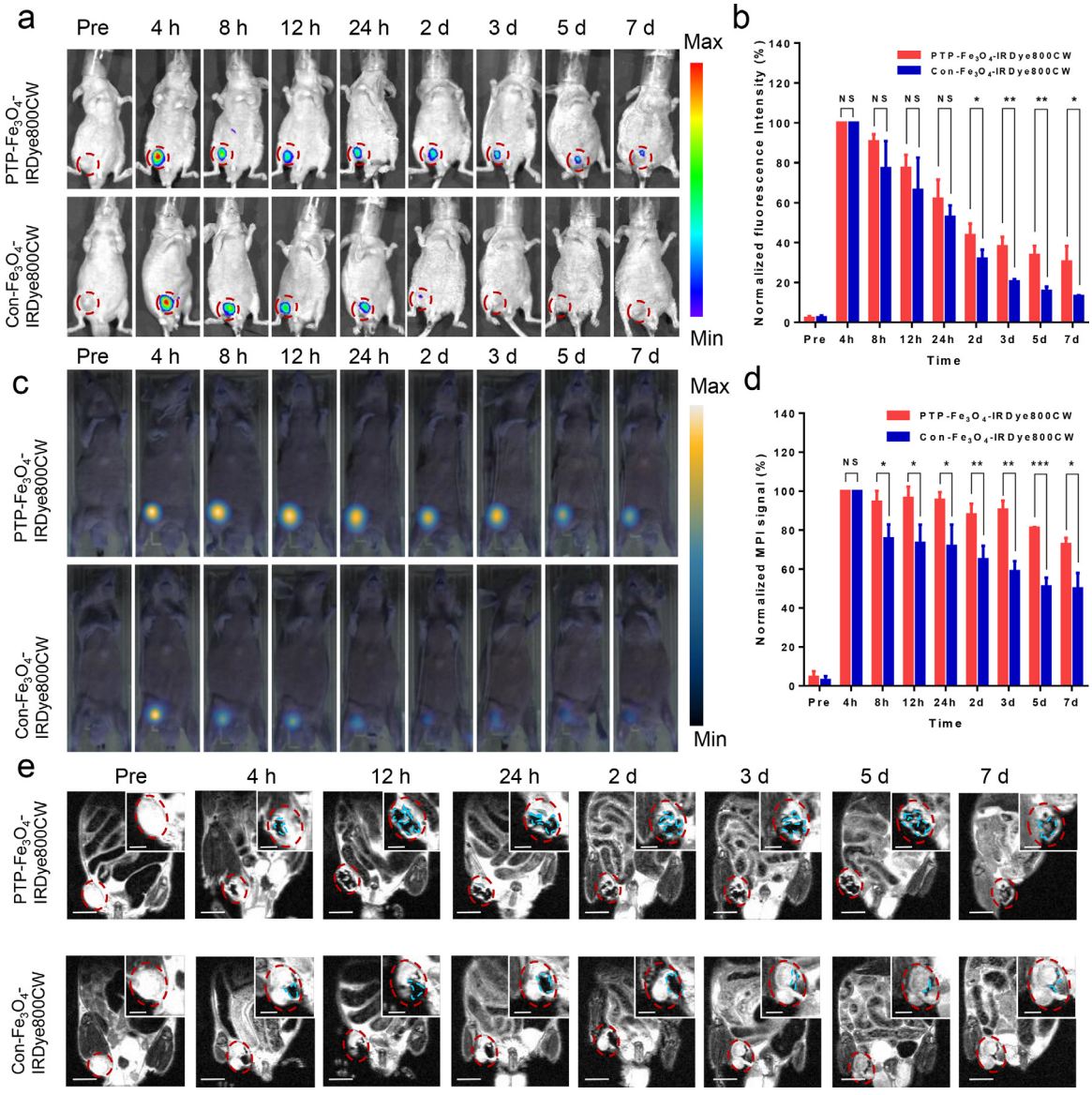

Figure 4. *In vivo* multimodality imaging of subcutaneous PDAC model. (a) Fluorescence images of subcutaneous mouse model *in vivo* at different time points. The red dotted circle represents the location of PDAC ($n = 3$). (b) Quantitative comparison of normalised fluorescence intensity of the nanoparticles ($n = 3$). (c) MPI images of subcutaneous PDAC mouse model *in vivo* at different time points ($n = 3$). (d) Quantitative comparison of normalised MPI signal of the nanoparticles ($n = 3$). (e) MRI images of subcutaneous mouse model *in vivo* at different time points ($n = 3$). The red dotted circle represents the location of PDAC. The blue dotted line drew the outline of nanoparticles area. Student's *t* test. *, $P < 0.05$; **, $P < 0.01$; ***, $P < 0.001$. (scale bar: 0.4 cm; scale bar in magnified pictures: 0.4 cm)

liver function. For renal function, serum creatinine (Scr) and blood urea nitrogen (BUN) levels were measured. There were no differences between the two groups and the healthy normal mice group (Supplementary Figure 4b).

***In vivo* MPI, FMI and MRI multimodality imaging for orthotopic PDAC mouse model.** Based on the above findings, we further performed targeted multimodality imaging of orthotopic PDAC, which can mimic the real tumour growth environment. The orthotopic model was established using Pano2-Luc cells, and BLI was carried out to confirm the successful establishment of the orthotopic model (Supplementary Figure 5a, b). The *in vivo* biodistribution and targeting specificity of the nanoparticles were investigated. The imaging nanoparticles were intratumourally injected, and MPI-FMI-MRI

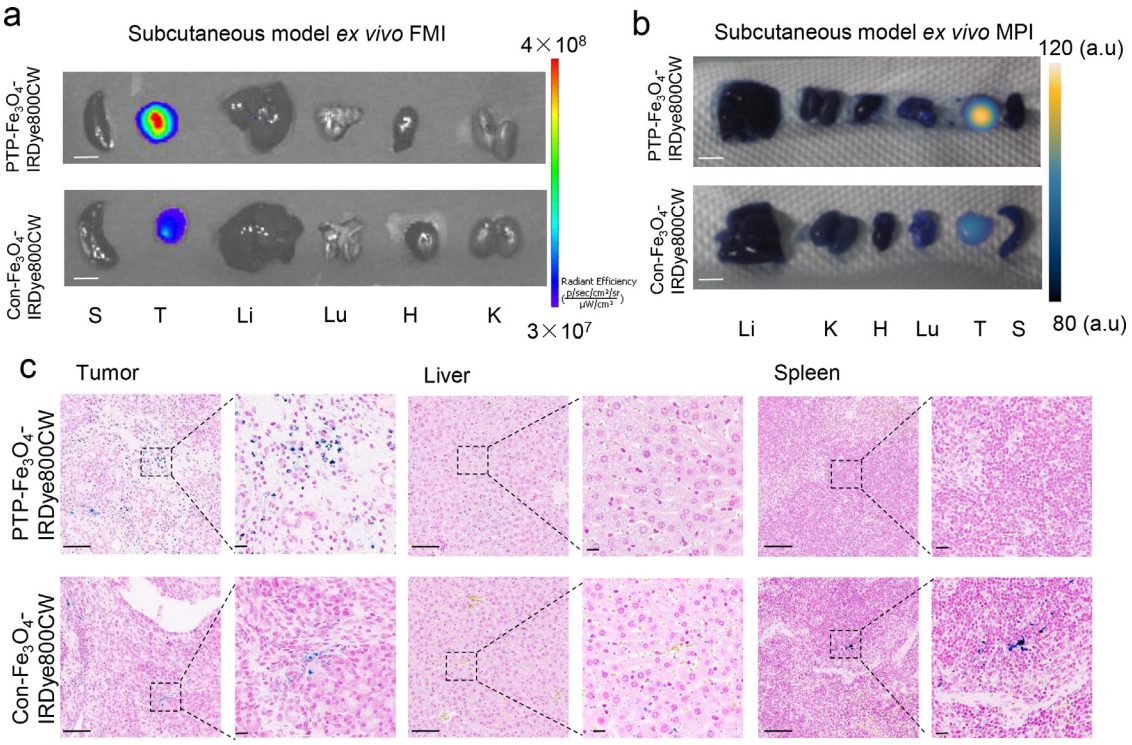

Figure 5. *Ex vivo* imaging of subcutaneous model and Prussian blue staining. *Ex vivo* fluorescence images (a) and MPI images (b) of resected tumours and major organs from the subcutaneous model at 2 d. S: spleen. T: tumour. Li: liver. H: heart. Lu: lung. K: kidney (scale bar: 0.4 cm). (c) Prussian blue staining of resected subcutaneous tumours, liver, and spleen (scale bar: 50 μm; scale bar in magnified pictures: 50 μm).

triple-modality imaging was then carried out dynamically. As shown in Figure 6a, FMI of both the PTP-Fe_3O_4-IRDye800CW and Con-Fe_3O_4-IRDye800CW groups (n = 3, respectively) showed the highest fluorescence signal at tumour sites at 4 h post-injection, after which the signal gradually decreased. The fluorescence signals in the PTP-Fe_3O_4-IRDye800CW group decreased more slowly compared to those in the Con-Fe_3O_4-IRDye800CW group. The difference in fluorescence intensity between two groups at the tumour site peaked at 2 d (PTP-Fe_3O_4-IRDye800CW group: 64.6% ± 7.03% vs. Con-Fe_3O_4-IRDye800CW group: 41.99% ± 0.12%, $^{**}P < 0.01$ (Student's t test)). Moreover, statistical difference of the fluorescence intensity between two groups could last for 7 d (PTP-Fe_3O_4-IRDye800CW group: 45.73% ± 6.42% vs. Con-Fe_3O_4-IRDye800CW group: 32.93% ± 0.76%, $^{*}P < 0.05$ (Student's t test)) (Figure 6b). However, FMI of deep tumours suffered from light scattering and limited imaging depth etc.[29] Therefore, MPI was further performed to overcome this problem.

MPI was further performed *in vivo*. As shown in Figure 6c and d, the two groups (n = 3, respectively) displayed different MPI signals at 2 d (PTP-Fe_3O_4-IRDye800CW group: 85.72 ± 1.53% vs. Con-Fe_3O_4-IRDye800CW group: 74.41 ± 1.91%, $^{**}P < 0.01$ (Student's t test)); While the signals in the PTP-Fe_3O_4-IRDye800CW group lasted for 7 d post-injection but not Con-Fe_3O_4-IRDye800CW group (68.78 ± 7.75% vs. 49.66 ± 7.39%, $^{*}P < 0.05$ (Student's t test)). Moreover, 3D MPI/CT images showed a more intense and homogeneous distribution of the PTP-Fe_3O_4-IRDye800CW nanoparticles (Supplementary Video 1) compared to the Con-Fe_3O_4-IRDye800CW nanoparticles (Supplementary Video 2) on the orthotopic tumours with details of the spatial positions of the whole body.

T2-weighted MRI was performed at the same time points. As shown in Figure 6e, the PTP-Fe_3O_4-IRDye800CW nanoparticles were distributed evenly inside tumours instead of being confined to the injection site as observed in the Con-Fe_3O_4-IRDye800CW group (n = 3, respectively) (red dotted circle showed the tumour *in situ*, blue dotted line indicated the outline of nanoparticles area). The MRI signals were consistent with the results of MPI and FMI.

To further verify the *in vivo* multimodality imaging observations, we collected the pancreas with the tumours and major organs (spleen, liver, lung, heart, and kidney) of the mice at 2 d and examined their signal intensity. For *ex vivo* FMI, the fluorescence signals of

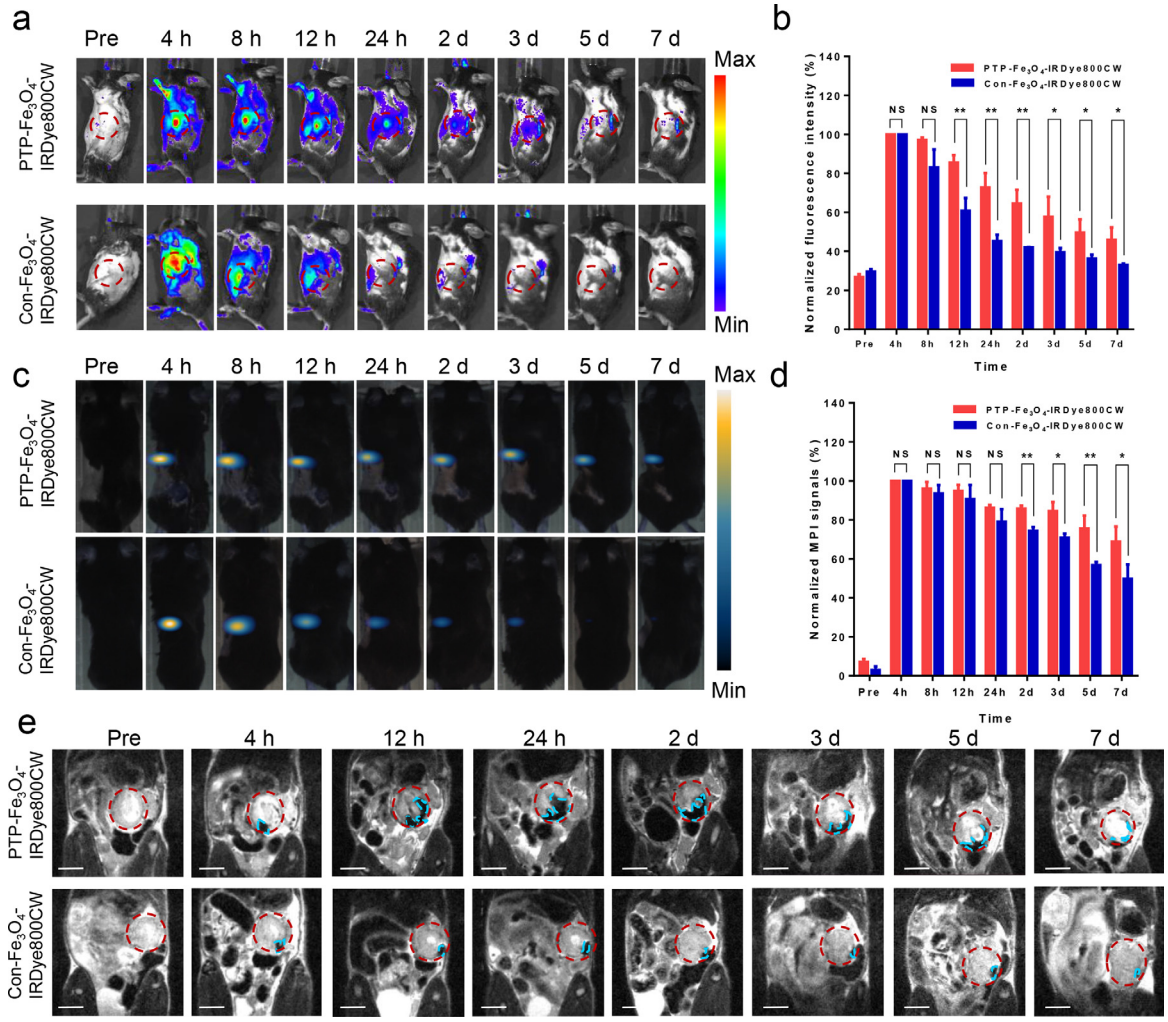

Figure 6. *In vivo* multimodality imaging of orthotopic PDAC model. (a) Fluorescence images of orthotopic mouse model *in vivo* at different time points. The red dotted circle represents the location of PDAC *in situ* ($n = 3$). (b) Quantitative comparison of normalized fluorescence intensity of the nanoparticles ($n = 3$). (c) MPI images of orthotopic mouse model *in vivo* at different time points ($n = 3$). (d) Quantitative comparison of normalised MPI signal of the nanoparticles ($n = 3$). (e) MRI images of orthotopic mouse model *in vivo* at different time points ($n = 3$). The red dotted circle represents the location of PDAC. The blue dotted line drew the outline of nanoparticles area. Student's *t* test. *, $P < 0.05$; **, $P < 0.01$; ***, $P < 0.001$. (scale bar: 0.4 cm; scale bar in magnified pictures: 0.4 cm)

tumours in the PTP-Fe_3O_4-IRDye800CW group were obvious stronger than those in the Con-Fe_3O_4-IRDye800CW group (Figure 7a). In addition, the *ex vivo* MPI signals were further validated the tumours of PTP-Fe_3O_4-IRDye800CW group showed higher MPI signals than those of the Con-Fe_3O_4-IRDye800CW group (PTP-Fe_3O_4-IRDye800CW: 30.13 ± 0.24 vs. Con-Fe_3O_4-IRDye800CW: 8.89 ± 1.03, ****$P < 0.0001$ (Student's *t* test)) (Supplementary Figure 3b)), suggesting that the PTP-Fe_3O_4-IRDye800CW group showed longer signal retention than the Con-Fe_3O_4-IRDye800CW group (Figure 7b). H&E and Prussian blue stainings results indicated more Fe-positive staining was within the tumour in the PTP-Fe_3O_4-IRDye800CW group than the Con-Fe_3O_4-IRDye800CW group (Figure 7c).

Discussion

In this study, PDAC targeted PTP-Fe_3O_4-IRDye800CW nanoparticles were developed as the targeted imaging probes for MPI, FMI and MRI triple-modality imaging of PDAC. This study used MPI for the deep and positive detection of PDAC, and the complementation with FMI/MRI can provide sensitive and high spatial resolution imaging signals. Multimodality imaging provides a potential strategy for the precise detection of PDAC

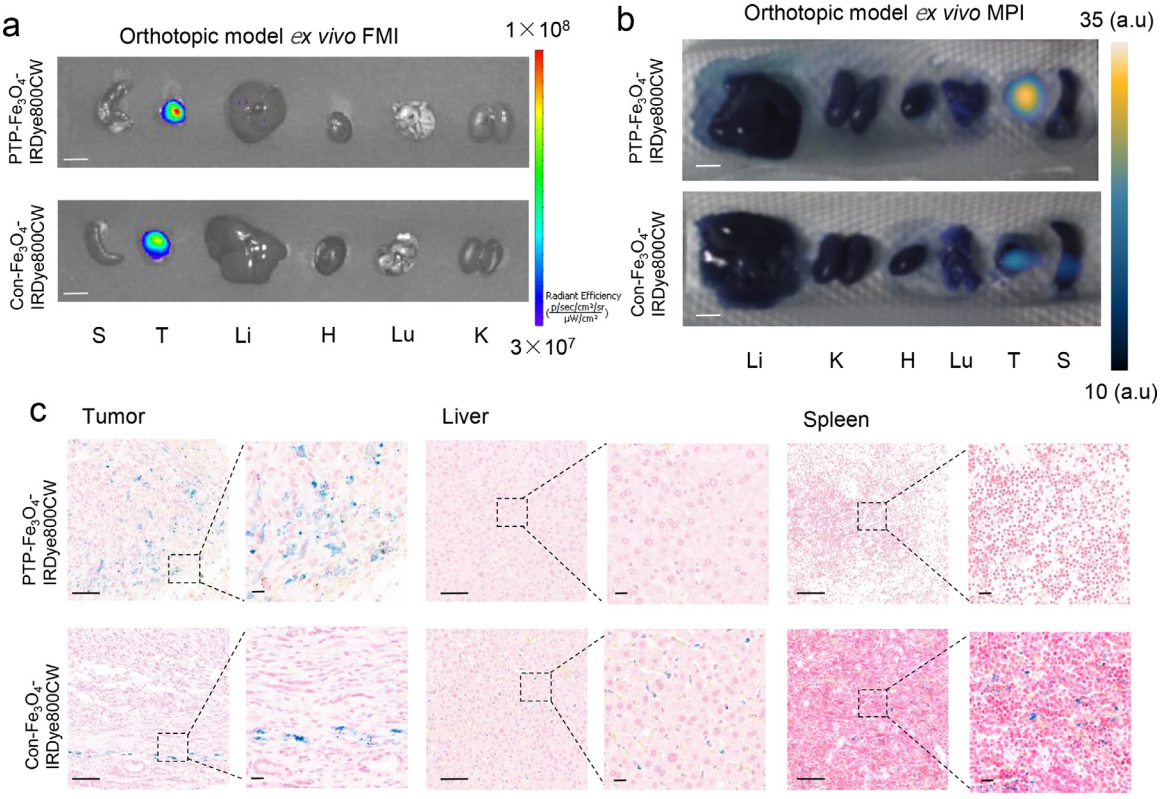

Figure 7. *Ex vivo* imaging of orthotopic PDAC model and Prussian blue staining. *Ex vivo* fluorescence images (a) and MPI images (b) of resected PDAC tumours and major organs from the orthotopic model at 2 d. S: spleen. T: tumour. Li: liver. H: heart. Lu: lung. K: kidney (scale bar: 0.4 cm). (c) Prussian blue staining of resected orthotopic tumours, liver, and spleen (scale bar: 50 μm; scale bar in magnified pictures: 50 μm).

at early stage and provides timely guidance for PDAC therapy.

Through the *in vivo* MPI and FMI, we concluded that the PTP-Fe_3O_4-IRDye800CW nanoparticles diffused more evenly inside the tumours than the Con-Fe_3O_4-IRDye800CW nanoparticles, thereby facilitating the detection of the whole tumour with clear delineation of the tumour margin. PTP-Fe_3O_4-IRDye800CW nanoparticles also exhibited longer retention at tumour sites, which can effectively guide therapy. Notably, the MRI images confirmed that the PTP-Fe_3O_4-IRDye800CW nanoparticles penetrated more uniformly, evenly, and effectively than Con-Fe_3O_4-IRDye800CW nanoparticles. This is mainly due to the driving force between the targeted binding of PTP peptide on the nanoparticles to the plectin-1 protein expressed on tumour cells. However, the Con-Fe_3O_4-IRDye800CW nanoparticles were mainly limited to the injection site and then were metabolized into blood and partly phagocytosed by reticuloendothelial-system. Notably, MPI enabled the longitudinal tracking of nanoparticles in a living mouse model for 7 d.

We mainly utilized the intratumoural injection for the *in vivo* imaging experiments. Intra-tumoural administration has been one of the delivery routes for the agents in the theranostics of PDAC. Zhu et al. reported that intratumoural injection of QM−HSP−CPP, an enzyme-activatable aggregation-induced-emission probe, allowed *in vivo* imaging and long-term tracking of PDAC via near-infrared fluorescence in a PDAC mouse model.[30] In addition, the intratumoural injection of chemicals in PDAC field (e.g. chemotherapeutics, ^{125}I) has become a hallmark of local cancer therapy.[31] In the immunotherapy of PDAC, nanomedicines can be developed to facilitate antitumour immune responses through a series of immuno-potentiating functions after being directly injected into tumours.[32,33] Immunotherapy drug through intratumoural injection in PDAC exerted prominent antitumour effects and resulted in tumour decrease in several clinical trials (NCT02045589; NCT03198546).[34,35] Moreover, intra-tumoural delivery of agents has also been reported in the application of other tumour types. In a prospective randomized phase II clinical study, intratumoural injection of a hybrid radioactive and fluorescent tracer contributes to detection of tumour-positive lymph nodes better than intraprostatic tracer injection for prostate tumour patients.[36] In the field of near-infrared tracer-guided radical gastrectomy, Chen et al. conducted a randomized

clinical trial, revealing that peritumoural injection of indocyanine green can significantly increase the number of lymph node dissections and decrease lymph node noncompliance without increased complications.[37,38] The application of intratumoural injection in tumours is attributed to its several advantages. Firstly, intratumoural injection can avoid low therapeutic index and increase imaging agent accumulation through intravenous injection. Second, this method can also reduce systemic exposure of imaging agent to avoid unnecessary toxicity.[39] Moreover, intratumoural injection method combined with anti-tumour therapy shows promising value of clinical translation.[33] In virtue of long-lasting accumulation of PTP-Fe_3O_4-IRDye800CW nanoparticles in PDAC, this method could assist in precise tumour excision and aid post-surgical or post-therapeutic follow-up imaging without further repetitive administration of contrast agents. Still, there are some limitations for this study. For example, the intratumoural injection may be at risk of metastasis, and different sizes of tumours may be injected with the corresponding volumes of imaging probes. Second, considering of loading therapeutic drugs for the MPI-guided theranostics of PDAC will be our future work direction.

Several types of iron oxide nanoparticles have been developed and approved for clinical use: ferumoxytol, ferucarbotran and ferumoxides.[40] Among clinically available iron oxide nanoparticles, ferumoxytol has been applied in MRI, iron supplements, anti-cancer and anti-inflammatory therapies.[41,42] Compared with ferumoxytol, the PTP-Fe_3O_4-IRDye800CW nanoparticles in our study have several advantages. First, synthesized PTP-Fe_3O_4-IRDye800CW has the plectin-1 peptide, which allows its targeting ability to the PTP and pancreatic cancer cells; however, the surface coating of ferumoxytol is composed of glucose polysaccharide, which shows no targeting ability to cancers.[43] Second, the near-infrared dye and iron oxide of PTP-Fe_3O_4-IRDye800CW enable triple-modal imaging, including FMI, MPI and MRI, which can provide more comprehensive information for characterizing the tumour properties, while ferumoxytol is an MRI and MPI contrast imaging agent.[44] Third, although ferumoxytol has anti-cancer efficacy through altering the polarization of tumour associated macrophages,[40] PTP-Fe_3O_4-IRDye800CW has shown its heating efficacy under an alternating current magnetic field in our preliminary test (Supplementary Figure 6), indicating that PTP-Fe_3O_4-IRDye800CW has the potential application in the magnetic hyperthermia therapy for PDAC.

In conclusion, the combination of MPI with FMI/MRI triple-modality imaging can facilitate precision and high-resolution detection of orthotopic PDAC *in vivo*. Our triple-modality imaging approach for PDAC may have broad theranostic applications, such as sensitive tumour detection, delineation of tumour margin for intraoperative surgery, post-surgical follow-up imaging without repetitive administration of contrast agents, and guidance for targeted therapy such as magnetic hyperthermia therapy. Moreover, the main components of PTP-Fe_3O_4-IRDye800CW nanoparticles are biocompatible materials, and hence, these nanoparticles possess potential for clinical translation for PDAC diagnosis and therapy in the future.

Contributors

Literature search: Wenjia Zhang, Yang Du, Xiaolong Liang, Liang Zhu, Xinyu Zhang

Figures: Wenjia Zhang, Xiaolong Liang, Yang Du

Study design: Wenjia Zhang, Yang Du, Xiaolong Liang

Data collection: Wenjia Zhang, Xiaolong Liang, Liang Zhu, Xinyu Zhang

Data analysis: all authors

Data interpretation: all authors

Writing: all authors

Access and verification of the data: all authors

Responsibilities for the decision to submit the manuscript: all authors.

Data sharing statement

The main data supporting the results of this study are available within the paper and its Supplementary materials. The raw FMI/MRI/MPI images can be obtained after asking for the corresponding authors and clarifying purpose of use.

Declaration of interests

The authors declare no conflicts of interests.

Acknowledgments

This study was funded by the National Natural Science Foundation of China (Grant No. 62027901, 82071896, 81871422, 81871514, 81227901), Ministry of Science and Technology of China under Grant No. 2017YFA0205200, 2017YFA0700401, Beijing Natural Science Foundation (Grant No. 7212207), Elite Program of Dong Cheng District of Beijing (2020-dchrcpyzz-28), and Peking University Third Hospital (BYSYZD2019018, and jyzc2018-02).

Supplementary materials

Supplementary material associated with this article can be found in the online version at doi:10.1016/j.ebiom.2022.104040.

References

1 Siegel RL, Miller KD, Jemal A. Cancer statistics, 2020. *CA Cancer J Clin*. 2020;70(1):7–30.

2 Willett CG, Czito BG, Bendell JC, Ryan DP. Locally advanced pancreatic cancer. *J Clin Oncol*. 2005;23(20):4538–4544.
3 Zeng S, Pottler M, Lan B, Grutzmann R, Pilarsky C, Yang H. Chemoresistance in pancreatic cancer. *Int J Mol Sci*. 2019;20(18):4504.
4 Eser S, Messer M, Eser P, et al. *In vivo* diagnosis of murine pancreatic intraepithelial neoplasia and early-stage pancreatic cancer by molecular imaging. *Proc Natl Acad Sci U S A*. 2011;108(24):9945–9950.
5 Hu Y, Chi C, Wang S, et al. A comparative study of clinical intervention and interventional photothermal therapy for pancreatic cancer. *Adv Mater*. 2017;29(33):1700448.
6 Lee GY, Qian WP, Wang L, et al. Theranostic nanoparticles with controlled release of gemcitabine for targeted therapy and MRI of pancreatic cancer. *ACS Nano*. 2013;7(3):2078–2089.
7 Watabe T, Liu Y, Kaneda-Nakashima K, et al. Theranostics targeting fibroblast activation protein in the tumor stroma: (64)Cu- and (225)Ac-labeled FAPI-04 in pancreatic cancer xenograft mouse models. *J Nucl Med*. 2020;61(4):563–569.
8 Song G, Zheng X, Wang Y, Xia X, Chu S, Rao J. A magneto-optical nanoplatform for multimodality imaging of tumors in mice. *ACS Nano*. 2019;13(7):7750–7758.
9 Sherry AD, Woods M. Chemical exchange saturation transfer contrast agents for magnetic resonance imaging. *Annu Rev Biomed Eng*. 2008;10:391–411.
10 Lazaro-Carrillo A, Filice M, Guillen MJ, et al. Tailor-made PEG coated iron oxide nanoparticles as contrast agents for long lasting magnetic resonance molecular imaging of solid cancers. *Mater Sci Eng C Mater Biol Appl*. 2020;107: 110262.
11 Gleich B, Weizenecker J. Tomographic imaging using the nonlinear response of magnetic particles. *Nature*. 2005;435(7046):1214–1217.
12 Yu EY, Bishop M, Zheng B, et al. Magnetic particle imaging: a novel *in vivo* imaging platform for cancer detection. *Nano Lett*. 2017;17(3):1648–1654.
13 Talebloo N, Gudi M, Robertson N, Wang P. Magnetic particle imaging: current applications in biomedical research. *J Magn Reson Imaging*. 2020;51(6):1659–1668.
14 Wu L, Mendoza-Garcia A, Li Q, Sun S. Organic phase syntheses of magnetic nanoparticles and their applications. *Chem Rev*. 2016;116(18):10473–10512.
15 Goodwill PW, Saritas EU, Croft LR, et al. X-space MPI: magnetic nanoparticles for safe medical imaging. *Adv Mater*. 2012;24(28):3870–3877.
16 Zhang X, Zeng Z, Liu H, et al. Recent development of a magneto-optical nanoplatform for multimodality imaging of pancreatic ductal adenocarcinoma. *Nanoscale*. 2022;14(9):3306–3323.
17 Jiang Z, Han X, Du Y, et al. Mixed metal metal-organic frameworks derived carbon supporting $ZnFe_2O_4$/C for high-performance magnetic particle imaging. *Nano Lett*. 2021;21(7):2730–2737.
18 Du Y, Liu X, Liang Q, Liang XJ, Tian J. Optimization and design of magnetic ferrite nanoparticles with uniform tumor distribution for highly sensitive MRI/MPI performance and improved magnetic hyperthermia therapy. *Nano Lett*. 2019;19(6):3618–3626.
19 Bulte JW. *In vivo* MRI cell tracking: clinical studies. *AJR Am J Roentgenol*. 2009;193(2):314–325.
20 Rosen JE, Chan L, Shieh DB, Gu FX. Iron oxide nanoparticles for targeted cancer imaging and diagnostics. *Nanomedicine*. 2012;8(3):275–290.
21 Briley-Saebo K, Bjornerud A, Grant D, Ahlstrom H, Berg T, Kindberg GM. Hepatic cellular distribution and degradation of iron oxide nanoparticles following single intravenous injection in rats: implications for magnetic resonance imaging. *Cell Tissue Res*. 2004;316(3):315–323.
22 Hsieh WJ, Liang CJ, Chieh JJ, et al. *In vivo* tumor targeting and imaging with anti-vascular endothelial growth factor antibody-conjugated dextran-coated iron oxide nanoparticles. *Int J Nanomedicine*. 2012;7:2833–2842.
23 Jie LY, Cai LL, Wang LJ, et al. Actively-targeted LTVSPWY peptide-modified magnetic nanoparticles for tumor imaging. *Int J Nanomedicine*. 2012;7:3981–3989.
24 Kumar M, Singh G, Arora V, et al. Cellular interaction of folic acid conjugated superparamagnetic iron oxide nanoparticles and its use as contrast agent for targeted magnetic imaging of tumor cells. *Int J Nanomedicine*. 2012;7:3503–3516.
25 Kelly KA, Bardeesy N, Anbazhagan R, et al. Targeted nanoparticles for imaging incipient pancreatic ductal adenocarcinoma. *PLoS Med*. 2008;5(4):e85.
26 Bausch D, Thomas S, Mino-Kenudson M, et al. Plectin-1 as a novel biomarker for pancreatic cancer. *Clin Cancer Res*. 2011;17(2):302–309.
27 Glazer AN. Bioconjugate techniques - Hermanson, GT. *Nature*. 1996;381(6580):290.
28 Natarajan A, Mayer AT, Xu L, Reeves RE, Gano J, Gambhir SS. Novel radiotracer for ImmunoPET imaging of PD-1 checkpoint expression on tumor infiltrating lymphocytes. *Bioconjug Chem*. 2015;26(10):2062–2069.
29 Kwon S, Sevick-Muraca EM. Effects of depilation-induced skin pigmentation and diet-induced fluorescence on *in vivo* fluorescence imaging. *Contrast Media Mol Imaging*. 2017;2017: 7659242.
30 Zhu Z, Wang Q, Chen X, et al. An enzyme-activatable aggregation-induced-emission probe: intraoperative pathological fluorescent diagnosis of pancreatic cancer via specific cathepsin E. *Adv Mater*. 2022;34:(3) e2107444.
31 Ahmed M, Solbiati L, Brace CL, et al. Image-guided tumor ablation: standardization of terminology and reporting criteria—a 10-year update. *Radiology*. 2014;273(1):241–260.
32 Kato H, Huang X, Kadonaga Y, et al. Intratumoral administration of astatine-211-labeled gold nanoparticle for alpha therapy. *J Nanobiotechnol*. 2021;19(1):223.
33 Cabral H, Kinoh H, Kataoka K. Tumor-targeted nanomedicine for immunotherapy. *Acc Chem Res*. 2020;53(12):2765–2776.
34 Bazan-Peregrino M, Garcia-Carbonero R, Laquente B, et al. VCN-01 disrupts pancreatic cancer stroma and exerts antitumor effects. *J Immunother Cancer*. 2021;9(11):e003254.
35 Pang N, Shi J, Qin L, et al. IL-7 and CCL19-secreting CAR-T cell therapy for tumors with positive glypican-3 or mesothelin. *J Hematol Oncol*. 2021;14(1):118.
36 Wit EMK, van Beurden F, Kleinjan GH, et al. The impact of drainage pathways on the detection of nodal metastases in prostate cancer: a phase II randomized comparison of intratumoral vs intraprostatic tracer injection for sentinel node detection. *Eur J Nucl Med Mol Imaging*. 2022;49(5):1743–1753.
37 Achterberg FB, Deken MM, Meijer RPJ, et al. Clinical translation and implementation of optical imaging agents for precision image-guided cancer surgery. *Eur J Nucl Med Mol Imaging*. 2021;48(2):332–339.
38 Chen QY, Xie JW, Zhong Q, et al. Safety and efficacy of indocyanine green tracer-guided lymph node dissection during laparoscopic radical gastrectomy in patients with gastric cancer: a randomized clinical trial. *JAMA Surg*. 2020;155(4):300–311.
39 Melero I, Castanon E, Alvarez M, Champiat S, Marabelle A. Intratumoural administration and tumour tissue targeting of cancer immunotherapies. *Nat Rev Clin Oncol*. 2021;18(9):558–576.
40 Huang Y, Hsu JC, Koo H, Cormode DP. Repurposing ferumoxytol: diagnostic and therapeutic applications of an FDA-approved nanoparticle. *Theranostics*. 2022;12(2):796–816.
41 Miller MA, Gadde S, Pfirschke C, et al. Predicting therapeutic nanomedicine efficacy using a companion magnetic resonance imaging nanoparticle. *Sci Transl Med*. 2015;7(314):314ra183.
42 Ramanathan RK, Korn RL, Raghunand N, et al. Correlation between ferumoxytol uptake in tumor lesions by MRI and response to nanoliposomal irinotecan in patients with advanced solid tumors: a pilot study. *Clin Cancer Res*. 2017;23(14):3638–3648.
43 Neiser S, Rentsch D, Dippon U, et al. Physico-chemical properties of the new generation IV iron preparations ferumoxytol, iron isomaltoside 1000 and ferric carboxymaltose. *Biometals*. 2015;28(4):615–635.
44 Nejadnik H, Pandit P, Lenkov O, Lahiji AP, Yerneni K, Daldrup-Link HE. Ferumoxytol can be used for quantitative magnetic particle imaging of transplanted stem cells. *Mol Imaging Biol*. 2019;21(3):465–472.